Investigating the Potential for Super-Resolution in Digital Breast Tomosynthesis

Raymond J. Acciavatti and Andrew D. A. Maidment
University of Pennsylvania, Department of Radiology, 3400 Spruce St., Philadelphia PA 19104
E-mail: racci@seas.upenn.edu and Andrew.Maidment@uphs.upenn.edu

ABSTRACT

Digital breast tomosynthesis (DBT) is an emerging 3D x-ray imaging modality in which tomographic sections of the breast are generated from a limited range of tube angles. Because non-normal x-ray incidence causes the image of an object to be translated in sub-pixel increments with increasing projection angle, it is demonstrated in this work that DBT is capable of super-resolution (*i.e.*, sub-pixel resolution). The feasibility of super-resolution is shown with a commercial DBT system using a bar pattern phantom. In addition, a framework for investigating super-resolution analytically is proposed by calculating the reconstruction profile for a sine input whose frequency is greater than the alias frequency of the detector. To study the frequency spectrum of the reconstruction, its continuous Fourier transform is also calculated. It is shown that the central projection cannot properly resolve frequencies higher than the alias frequency of the detector. Instead, the central projection represents a high frequency signal as if it were a lower frequency signal. The Fourier transform of the central projection is maximized at this lower frequency and has considerable spectral leakage as evidence of aliasing. By contrast, simple backprojection can be used to image high frequencies properly. The Fourier transform of simple backprojection is correctly maximized at the input frequency. Adding filters to the simple backprojection reconstruction smoothens pixilation artifacts, and reduces spectral leakage found in the frequency spectrum. In conclusion, this work demonstrates the feasibility of super-resolution in DBT experimentally and provides a framework for characterizing its presence analytically.

Keywords: Digital breast tomosynthesis (DBT), bar pattern phantom, aliasing, super-resolution, image reconstruction, filtered backprojection (FBP), Fourier transform, spectral leakage.

1. INTRODUCTION

Digital breast tomosynthesis (DBT) is a 3D imaging modality in which projections of the compressed breast are acquired over a limited range of x-ray tube angles. Using digital image reconstruction techniques, tomographic sections can be generated at all depths of the breast volume. Preliminary studies have demonstrated that DBT has greater sensitivity and specificity for early cancer detection in women relative to conventional 2D digital mammography (DM) [1].

In DBT, the projection images are sampled by a digital detector before being filtered and backprojected to generate the reconstruction. Because the samplings differ by sub-pixel increments, it will be demonstrated in this work that DBT has the potential for super-resolution (*i.e.*, sub-pixel resolution). Super-resolution is a term which describes the ability to resolve frequencies higher than the alias frequency of the detector, or the frequency above which high frequency information is represented as if it were low frequency information. Super-resolution has been well-described in a number of applications involving reconstruction from projections [2], including forensics, satellite imaging, computerized tomography (CT), and magnetic resonance imaging (MRI), but to our knowledge, its potential in DBT has not yet been identified.

In breast imaging, super-resolution has applications in the visualization of small microcalcification clusters which are an early indication of cancer. As a result, an understanding of super-resolution and an analysis of how to optimize its presence may prove to be important for designing the highest quality DBT systems. Although it would seem easy to improve spatial resolution simply by reducing the pixel size, there are practical limits as to the smallest pixel size that can be manufactured. In addition, smaller pixels generate increased shot noise that lowers image quality, and the number of photons per pixel is reduced.

Using a lead phantom with etched line pairs (lp), we have experimentally verified the feasibility of super-resolution in DBT. The bar patterns range in frequency from 1 lp/mm to 10 lp/mm in 1 lp/mm increments, and each frequency spans a 6.0 mm length. The lead phantom was taped underneath the compression paddle (18.0 cm × 24.0 cm) of a Selenia Dimensions integrated multi-mode mammography and tomosynthesis x-ray system (Hologic Inc., Bedford, MA) and placed 4.0 cm above the breast support. With the phantom positioned at an approximately 3° angle relative to the detector lattice, 15 projections were acquired at 30 kV and 14 mAs with a W/Al target-filter combination and a 0.3 mm focal spot. The mAs setting was determined after acquiring photo-timed images of the phantom positioned on top of stacked acrylic blocks of varying thicknesses (2.0, 4.0, and 6.0 cm). The optimal mAs for imaging the bar pattern phantom alone was found by fitting the photo-timed mAs versus the acrylic thickness and then extrapolating for 0 cm acrylic thickness (graph not shown).

Reconstruction was subsequently performed using a commercial backprojection filtering (BPF) algorithm developed by Real Time Tomography, LLC (Villanova, PA). The filter parameters were representative of those used clinically. In the plane of reconstruction, the pixel size of the reconstruction grid (11.5 μm) was specified to be considerably smaller than that of the detector elements (140 μm), so that the alias frequency of the reconstruction grid (43.5 lp/mm) was significantly higher than the alias frequency of the detector (3.57 lp/mm).
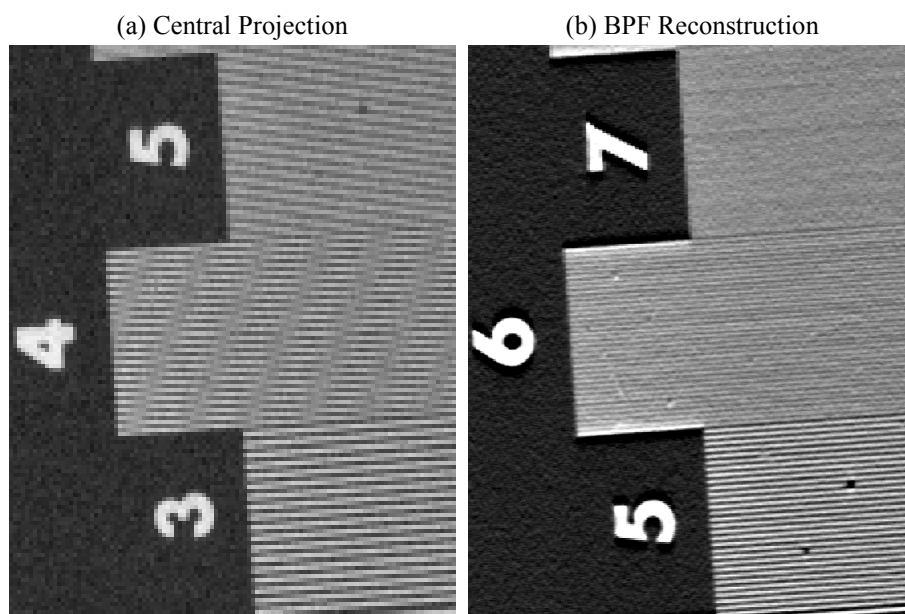
(a) Central Projection   (b) BPF Reconstruction

Figure 1. A lead bar pattern phantom was imaged with a Selenia Dimensions x-ray unit. The BPF reconstruction (right image) can clearly distinguish higher spatial frequencies that the central projection (left image), providing experimental evidence of DBT's potential for super-resolution.

As shown in Figure 1, one can clearly see frequencies up to 3 lp/mm in the central projection without any evidence of aliasing. This finding is expected, since these frequencies are smaller than the alias frequency $0.5a^{-1}$ (3.57 lp/mm), where a denotes the detector element length (140 μm). At the next highest frequency, 24 line pairs spanning 6.0 mm can be observed, accurately corresponding to 4 lp/mm; however, their orientation is skewed and Moiré patterns [3] are present. Finally, at 5 lp/mm, fewer line pairs are resolved than expected and the line pairs are displayed at an erroneous oblique orientation, indicating that the pattern is aliased.

By contrast, the BPF reconstruction clearly resolves frequencies higher than the detector alias frequency of 3.57 lp/mm. In fact, up to 6 lp/mm (36 line pairs spanning 6.0 mm) can be observed at the correct orientation with no Moiré pattern. At 7 lp/mm, however, the signal is too faint to distinguish the pattern. This finding arises from the fact that the modulation of the reconstruction is reduced at higher frequencies.

2. METHODS

2.1 Projection Images of a Sinusoidal Input

An analytical framework for investigating DBT's potential for super-resolution is now proposed by studying the reconstruction of a sinusoidal input whose frequency is greater than the alias frequency of the detector. Accordingly, suppose that a 2D rectangular sheet with infinite extent in the $+x$ and $-x$ directions has a linear attenuation coefficient $\mu(x, z)$ which varies sinusoidally with position x. Although an actual input to a clinical breast imaging system would be 3D, a 2D construct is a useful pedagogical tool for modeling detector measurements along the chest wall. A study of measurements made in directions perpendicular to the chest wall is reserved for future work. As shown in Figure 2, the rectangular sheet is positioned between $z = z_0 - \varepsilon/2$ and $z = z_0 + \varepsilon/2$, where z_0 is the central height of the sheet above the detector and ε is the sheet's thickness. The frequency of the waveform may be denoted ν_0, and its translational shift relative to the origin O (*i.e.*, the center of the detector) may be denoted x_0.

$$\mu(x,z) = \frac{\cos[2\pi\nu_0(x - x_0)]}{\varepsilon} \cdot \text{rect}\left(\frac{z - z_0}{\varepsilon}\right), \qquad \text{rect}(u) \equiv \begin{cases} 1 & , |u| \leq 1/2 \\ 0 & , |u| > 1/2 \end{cases} \tag{1}$$

For convenience, the attenuation coefficient is normalized by a factor of $1/\varepsilon$ so that the total attenuation found by integrating along the z direction is simply $\cos[2\pi\nu_0(x - x_0)]$ for all ε. Provided that $|z - z_0| \leq \varepsilon$, the continuous Fourier transform ($\mathcal{F}$) of Eq. (1) along the x direction peaks at the frequencies $\nu = \pm\nu_0$ and vanishes at all other frequencies [4].

$$\mathcal{F}\mu(\nu, z) = \int_{-\infty}^{\infty} \mu(x, z) \cdot e^{-2\pi i \nu x} dx = \left[\frac{e^{2\pi i \nu_0 x_0}}{2\varepsilon}\delta(\nu + \nu_0) + \frac{e^{-2\pi i \nu_0 x_0}}{2\varepsilon}\delta(\nu - \nu_0)\right] \cdot \text{rect}\left(\frac{z - z_0}{\varepsilon}\right) \tag{2}$$

Typically, only the positive frequency is of interest in an experimental measurement. Thus, although it is non-physical for an attenuation coefficient to vary between negative and positive values, formulating $\mu(x, z)$ by Eq. (1) is helpful for a thought experiment in interrogating the reconstruction of a single input frequency.

Super-resolution in DBT arises because sub-pixel shifts in the image of the object occur with increasing projection angle. The translational shift for each projection is now determined from the x-ray acquisition geometry diagrammed schematically in Figure 2. The most general case of a divergent x-ray beam and a rotating detector is analyzed.
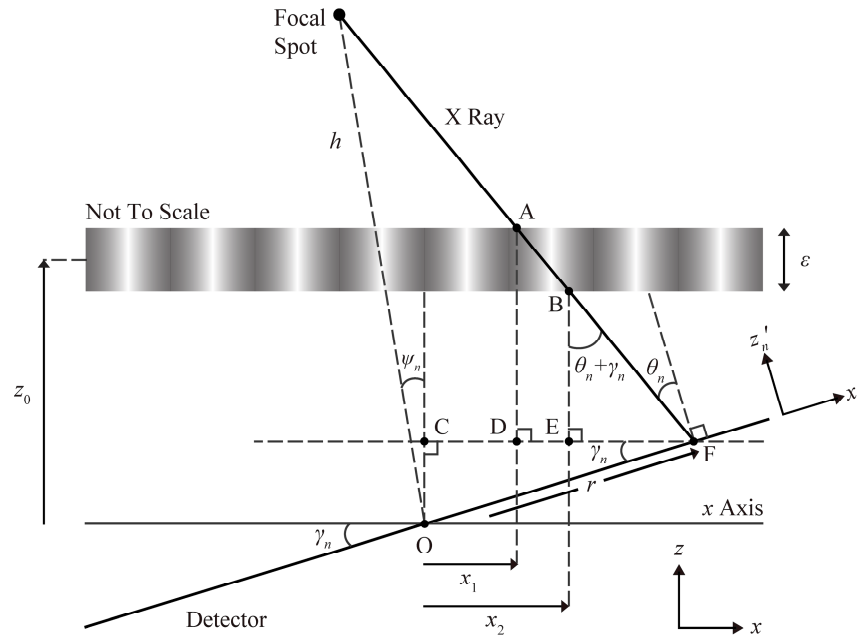

Figure 2. A schematic diagram of the DBT acquisition geometry for a divergent x-ray beam and a rotating detector is shown. The input has a linear attenuation coefficient which varies sinusoidally along the direction of the chest wall.

In acquiring the nth projection image, the point-like x-ray source rotates around the midpoint of the detector with the nominal projection angle ψ_n, and the detector rotates at the angle γ_n relative to the same point. The two parameters ψ_n and γ_n are determined from the nominal angular spacing $\Delta\psi$ and the detector gear ratio g by the relations

$$\psi_n = n \cdot \Delta\psi, \qquad \gamma_n = \frac{\psi_n}{g}. \tag{3}$$

For N total projections, the index n varies from $-(N-1)/2$ to $(N-1)/2$, and the special case $n = 0$ defines the central projection. Positive directionalities of the angle of x-ray incidence and the rotation of the detector are defined as the ones shown in Figure 2. Now, in applying trigonometry to triangles BEF, ADF, and CFO, one finds

$$\overline{\text{EF}} = \left(z_0 - \frac{\varepsilon}{2} - r\sin\gamma_n\right)\tan(\theta_n + \gamma_n), \qquad \overline{\text{DF}} = \left(z_0 + \frac{\varepsilon}{2} - r\sin\gamma_n\right)\tan(\theta_n + \gamma_n), \qquad \overline{\text{CF}} = r\cos\gamma_n, \tag{4}$$

where r measures position along the detector relative to the COR. Assuming that x rays travel in straight lines from the point of creation to the point of incidence on the detector, one can show that the angle of incidence θ_n relative to the normal to the detector varies with r as

$$\theta_n = -\gamma_n + \arctan\left(\frac{h\sin\psi_n + r\cos\gamma_n}{h\cos\psi_n - r\sin\gamma_n}\right), \tag{5}$$

where h is the source-to-COR distance. The displacements x_1 and x_2 in Figure 2 can therefore be determined from the relations

$$x_1 = \overline{\text{CF}} - \overline{\text{DF}} = \rho_n r - \lambda_n^+, \qquad x_2 = \overline{\text{CF}} - \overline{\text{EF}} = \rho_n r - \lambda_n^-, \tag{6}$$

where

$$\rho_n \equiv \cos\gamma_n + \sin(\gamma_n)\tan(\theta_n + \gamma_n), \qquad \lambda_n^\pm \equiv \left(z_0 \pm \frac{\varepsilon}{2}\right)\tan(\theta_n + \gamma_n). \tag{7}$$

Importantly, x_1 and x_2 define the x coordinates of the entrance and exit points of the x ray traveling through the object and thus determine the path length $\mathcal{L}_n$ for the nth projection. Total attenuation may now be calculated as

$$\int_{\mathcal{L}_n} \mu \, ds = \int_{x_1}^{x_2} \frac{\cos\left[2\pi v_0(x - x_0)\right]}{\varepsilon} \cdot \csc(\theta_n + \gamma_n)dx \tag{8}$$

$$= \frac{\csc(\theta_n + \gamma_n)}{2\pi v_0 \varepsilon} \cdot \left[\sin\left[2\pi v_0(\rho_n r - \lambda_n^- - x_0)\right] - \sin\left[2\pi v_0(\rho_n r - \lambda_n^+ - x_0)\right]\right]. \tag{9}$$

Eq. (9) provides an expression for signal intensity versus position r along the detector, assuming that the detector is non-pixilated and has a modulation transfer function (MTF) of unity at all frequencies and all values of θ_n. An amorphous selenium (a-Se) photoconductor operated in drift mode is a good approximation for a detector with these properties. To justify this claim, recall the analytical model of a-Se proposed by Que and Rowlands [5]. Their work calculates the MTF degradation that occurs at each frequency with increasing projection angle, and demonstrates that the degradation is minimal for detector positions along the chest wall. For example, using their model, one can show that the MTF at the corner of the chest wall side of the detector ($\theta_n = 11.6°$) in the Selenia Dimensions system for 200 μm thick a-Se is 96.6% at 5.0 lp/mm assuming 20 keV x rays. Since the angle of incidence deviates less considerably from the normal at positions closer to the COR, the MTF must be no smaller than 96.6% at all values of r. Consequently, for the purpose of this work, it is reasonable to neglect the MTF degradation that occurs due to oblique x-ray incidence on the detector.

In a clinical setting, the a-Se x-ray converter is often placed in electrical contact with a large area plate of amorphous silicon (a-Si) in which a thin-film transistor (TFT) array samples the detector signal in pixels (*i.e.*, detector elements). Using Eq. (9), the logarithmically-transformed signal in the mth detector element for the nth projection is calculated as

$$\mathcal{D}\mu(m,n) = \int_{a(m-1/2)}^{a(m+1/2)} \left[\int_{\mathcal{L}_n} \mu \, ds \right] \cdot \frac{dr}{a}, \tag{10}$$

where a denotes the length of the detector elements, which are taken to be centered on $r = ma$. The detector element at the center of rotation (COR) may be defined as the one corresponding to $m = 0$. Because the angle of incidence varies minimally along the length of a single detector element, the integral of Eq. (10) can be calculated by approximating the angle of incidence θ_n with its value at the center of the detector element. Under this approximation, it follows that

$$\mathcal{D}\mu(m,n) = \frac{\csc(\theta_{mn} + \gamma_n)}{4\pi^2 v_0^2 a \varepsilon \rho_{mn}} \cdot \begin{bmatrix} \cos\left[2\pi v_0 \left(a\rho_{mn}(m+1/2) - \lambda_{mn}^+ - x_0 \right) \right] + \cos\left[2\pi v_0 \left(a\rho_{mn}(m-1/2) - \lambda_{mn}^- - x_0 \right) \right] \\ -\cos\left[2\pi v_0 \left(a\rho_{mn}(m-1/2) - \lambda_{mn}^+ - x_0 \right) \right] - \cos\left[2\pi v_0 \left(a\rho_{mn}(m+1/2) - \lambda_{mn}^- - x_0 \right) \right] \end{bmatrix}, \tag{11}$$

where

$$\theta_{mn} \equiv \theta_n\big|_{r=ma}. \tag{12}$$

The quantities ρ_{mn}, and $\lambda_{mn}^{\pm}$ may be defined similarly by evaluation at $r = ma$. Hence, for the nth projection, the raw signal $\mathcal{S}\mu(r, n)$ and the Radon transform $\mathcal{R}\mu(t, n)$ are determined from

$$\mathcal{S}\mu(r,n) = \sum_m \mathcal{D}\mu(m,n) \cdot \text{rect}\left(\frac{r - ma}{a} \right), \qquad \mathcal{R}\mu(t,n) = \sum_m \mathcal{D}\mu(m,n) \cdot \text{rect}\left(\frac{t \sec\theta_{mn} - ma}{a} \right), \tag{13}$$

where t denotes the affine parameter [6, 7]. The Radon transform differs from the raw signal by the use of a secant term.

2.2 Filtered Backprojection (FBP) Reconstruction from the Projections

The reconstructed attenuation coefficient can now be determined by filtering the Radon transform with the function $\phi(t)$ and backprojecting the result along the angular ray of incidence [6, 7]. The specific formula for the filter $\phi(t)$ will be addressed in the next section. Assuming that the reconstruction grid is infinitesimally fine (*i.e.*, non-pixilated), the filtered backprojection (FBP) reconstruction is

$$\mu_{\text{FBP}}(x,z) = \mathcal{B}(\phi * \mathcal{R}\mu)(x,z) \tag{14}$$

$$= \frac{1}{N} \sum_m \sum_n \mathcal{D}\mu(m,n) \cdot \left[\phi(t) * \text{rect}\left(\frac{t \sec\theta_{mn} - ma}{a} \right) \right] \Bigg|_{t = x_n' \cos\theta_{mn} + z_n' \sin\theta_{mn}} \tag{15}$$

$$= \frac{1}{N} \sum_m \sum_n \mathcal{D}\mu(m,n) \cdot \left[\phi(t) * \text{rect}\left(\frac{t \sec\theta_{mn} - ma}{a} \right) \right] \Bigg|_{t = x \cos(\gamma_n + \theta_{mn}) + z \sin(\gamma_n + \theta_{mn})}. \tag{16}$$

In Eq. (14), μ_{FBP} denotes the reconstructed linear attenuation coefficient, $*$ denotes the convolution operator, and $\mathcal{B}$ denotes the backprojection operator. As shown in Eq. (15), backprojection may be performed for each of the n projections using the primed coordinate system in which the x_n' axis is parallel to the rotated detector and the z_n' axis is perpendicular to the rotated detector. The matrix transformation from the (x_n', z_n') coordinate system to the (x, z) coordinate system generates the transition from Eq. (15) to Eq. (16).

$$\begin{pmatrix} x_n' \\ z_n' \end{pmatrix} = \begin{pmatrix} \cos\gamma_n & \sin\gamma_n \\ -\sin\gamma_n & \cos\gamma_n \end{pmatrix} \begin{pmatrix} x \\ z \end{pmatrix} \tag{17}$$

A special case of Eq. (16) is simple backprojection (SBP) reconstruction.

$$\mathcal{B}(\mathcal{R}\mu)(x,z) = \frac{1}{N}\sum_m\sum_n \mathcal{D}\mu(m,n)\cdot\text{rect}\left[\frac{[x\cos(\gamma_n+\theta_{mn})+z\sin(\gamma_n+\theta_{mn})]\sec\theta_{mn}-ma}{a}\right] \tag{18}$$

With SBP, the filter ϕ effectively becomes a delta function in the spatial domain and a constant in the frequency domain.

2.3 Formulation of the Reconstruction Filter

Following Zhao's linear systems theory for DBT [8], a ramp (RA) filter should be applied to the Radon transform of each projection image to reduce the low frequency detector response [9]. The filter is truncated at the spatial frequencies $v = -\xi$ and $v = +\xi$ in the Fourier domain.

$$\mathcal{F}\phi_{\text{RA}}(v) = \begin{cases} |v| & , |v| \leq \xi \\ 0 & , |v| > \xi \end{cases} \tag{19}$$

The spatial representation $\phi_{\text{RA}}(t)$ of the RA filter is determined by its inverse Fourier transform [4].

$$\phi_{\text{RA}}(t) = \int_{-\infty}^{\infty}\mathcal{F}\phi_{\text{RA}}(v)\cdot e^{2\pi itv}dv = \frac{\pi\xi t\sin(2\pi\xi t)-\sin^2(\pi\xi t)}{\pi^2 t^2} \tag{20}$$

Using this result, the convolution in Eq. (16) can be calculated.

$$\phi_{\text{RA}}(t)*\text{rect}\left(\frac{t\sec\theta_{mn}-ma}{a}\right) = \frac{\left[\begin{array}{c}a\cos(\theta_{mn})\big[\cos(\pi a\xi\cos\theta_{mn})\cos[2\pi\xi(t-ma\cos\theta_{mn})]-1\big]\\ +2(t-ma\cos\theta_{mn})\sin(\pi a\xi\cos\theta_{mn})\sin[2\pi\xi(t-ma\cos\theta_{mn})]\end{array}\right]}{2\pi^2[t-(m-1/2)a\cos\theta_{mn}][t-(m+1/2)a\cos\theta_{mn}]} \tag{21}$$

Since noise tends to occur at high frequencies, a spectrum apodization (SA) filter is often applied in addition to the RA filter in order to reduce the high frequency detector response. Following Zhao's approach, we use a Hanning window function as the SA filter.

$$\mathcal{F}\phi_{\text{SA}}(v) = \begin{cases} \frac{1}{2}\left[1+\cos\left(\frac{\pi v}{\xi}\right)\right] & , |v| \leq \xi \\ 0 & , |v| > \xi \end{cases}, \qquad \phi_{\text{SA}}(t) = \frac{\sin(2\pi\xi t)}{2\pi t(1-4\xi^2 t^2)} \tag{22}$$

According to the convolution theorem [4], the net filter is thus

$$\phi_{\text{SA}}(t)*\phi_{\text{RA}}(t) = \frac{(12\xi^2 t^2-1)\sin^2(\pi\xi t)-\pi\xi t(4\xi^2 t^2-1)\sin(2\pi\xi t)-4\xi^2 t^2(4\xi^2 t^2+1)}{2\pi^2 t^2(2\xi t+1)^2(2\xi t-1)^2}. \tag{23}$$

The convolution of the net filter in Eq. (23) with the rect function in Eq. (16) can be performed in closed form similar to Eq. (21). For the sake of brevity, this result is omitted.

2.4 Fourier Spectra of the DBT Images

The continuous Fourier transform of the input waveform in the x direction peaks at the frequencies $v = \pm v_0$ and vanishes at all other frequencies provided that $|z - z_0| \leq \varepsilon$. To investigate whether the frequency spectra of the DBT images possess this expected dependency on v_0, continuous Fourier transforms may be calculated. The continuous Fourier transform of an individual projection is determined from Eq. (13) as

$$\mathcal{F}(\mathcal{S}\mu)(v,n) = \int_{-\infty}^{\infty}\mathcal{S}\mu(r,n)\cdot e^{-2\pi ivr}dr = a\cdot\text{sinc}(av)\cdot\sum_m\mathcal{D}\mu(m,n)\cdot e^{-2\pi imav}, \qquad \text{sinc}(u) \equiv \frac{\sin(\pi u)}{\pi u}, \tag{24}$$

and the continuous Fourier transform for SBP reconstruction is determined from Eq. (18) as

$$\mathcal{F}\big[\mathcal{B}(\mathcal{R}\mu)\big](v,z) = \frac{a}{N}\sum_m \sum_n \frac{\mathcal{D}\mu(m,n)\cdot\cos\theta_{mn}}{\cos(\gamma_n+\theta_{mn})}\cdot \text{sinc}\left[\frac{av\cos\theta_{mn}}{\cos(\gamma_n+\theta_{mn})}\right]\cdot e^{2\pi iv\left[z\tan(\gamma_n+\theta_{mn})-\frac{ma\cos\theta_{mn}}{\cos(\gamma_n+\theta_{mn})}\right]}. \tag{25}$$

To calculate the continuous Fourier transform for FBP reconstruction

$$\mathcal{F}\mu_{\text{FBP}}(v,z) = \frac{a}{N}\sum_m \sum_n \mathcal{F}\phi\big[v\sec(\gamma_n+\theta_{mn})\big]\cdot\frac{\mathcal{D}\mu(m,n)\cdot\cos\theta_{mn}}{\cos(\gamma_n+\theta_{mn})}\cdot \text{sinc}\left[\frac{av\cos\theta_{mn}}{\cos(\gamma_n+\theta_{mn})}\right]\cdot e^{2\pi iv\left[z\tan(\gamma_n+\theta_{mn})-\frac{ma\cos\theta_{mn}}{\cos(\gamma_n+\theta_{mn})}\right]}, \tag{26}$$

one must apply the convolution theorem in conjunction with Eq. (16).

3. RESULTS

DBT image acquisition is now simulated along the chest wall of a Selenia Dimensions detector with 15 projections taken at a nominal angular spacing ($\Delta\psi$) of 1.07°, assuming $h = 70.0$ cm, $x_0 = 0$ mm, $z_0 = 25.0$ mm, $\varepsilon = 0.5$ mm, $a = 140$ μm, and $v_0 = 0.7a^{-1}$ (5.0 lp/mm). To illustrate DBT's potential for super-resolution, the input frequency has been specified to be higher than the detector alias frequency $0.5a^{-1}$ (3.57 lp/mm). In addition, the distance z_0 has been chosen so that it corresponds to the central height within a 5.0 cm breast volume, which would be typical for many women.

3.1 Individual DBT Projections
In Figure 3, signal is plotted versus position r and the modulus of its Fourier transform is plotted versus frequency v for the central projection ($n = 0$) and the most oblique projection ($n = 7$). The two projections are similar in that they both represent a high frequency input as if it were a lower frequency input. For this reason, the major peak in the Fourier transform of a single projection does not occur at the input frequency 5.0 lp/mm but instead occurs at a lower frequency. Both projections also have considerable spectral leakage as evidence of aliasing.

The two DBT projections and their Fourier transforms are also plotted in Figure 3 for an infinite source-to-COR distance h with no change in the value of any of the other parameters. This limiting case is illustrative as it effectively transforms the divergent x-ray beam geometry into a parallel x-ray beam geometry. As such, the angle of incidence relative to the normal to the detector does not vary with position r by Eq. (5) but instead is always $\psi_n - \gamma_n$ for all values of r.

In the parallel beam geometry, the central projection represents the input frequency v_0 as if it were $a^{-1} - v_0$ or $0.3a^{-1}$. As a result, the Fourier transform has a major peak at the frequency $0.3a^{-1}$ (2.14 lp/mm), and has minor alias peaks at $0.7a^{-1}$ (5.0 lp/mm), $1.3a^{-1}$ (9.29 lp/mm), and $1.7a^{-1}$ (12.14 lp/mm). Unlike the parallel beam geometry, the divergent beam geometry magnifies the input so that its effective frequency is v_0/M, where M is the magnification. For a thin input object, the magnification is determined from the ratio of the source-to-COR distance to the source-to-object distance [10]. With $h = 70.0$ cm and $z_0 = 25.0$ mm, M is found to be 1.037.

$$M = \frac{h}{h - z_0} \tag{27}$$

As expected, Figure 3 demonstrates that the major peak of the Fourier transform for the divergent beam geometry occurs at $a^{-1} - v_0/M$ (2.32 lp/mm). The minor alias peaks occur at v_0/M (4.82 lp/mm), $2a^{-1} - v_0/M$ (9.46 lp/mm), and $a^{-1} + v_0/M$ (11.96 lp/mm). In short, the Fourier transform for the divergent beam geometry peaks at different frequencies than the parallel beam geometry. The Fourier peaks of the most oblique projection effectively occur at similar frequencies as the central projection.

3.2 SBP Image Reconstruction
In Figure 4, SBP reconstruction is performed at the height $z = z_0$, corresponding to the central value of z within the input object. Although a single projection is not capable of resolving the input frequency, SBP reconstruction is capable of representing 5.0 lp/mm properly. This property arises because the oblique projections give information about the input waveform which is not present in the central projection alone (Figure 3). The SBP Fourier transform correctly possesses
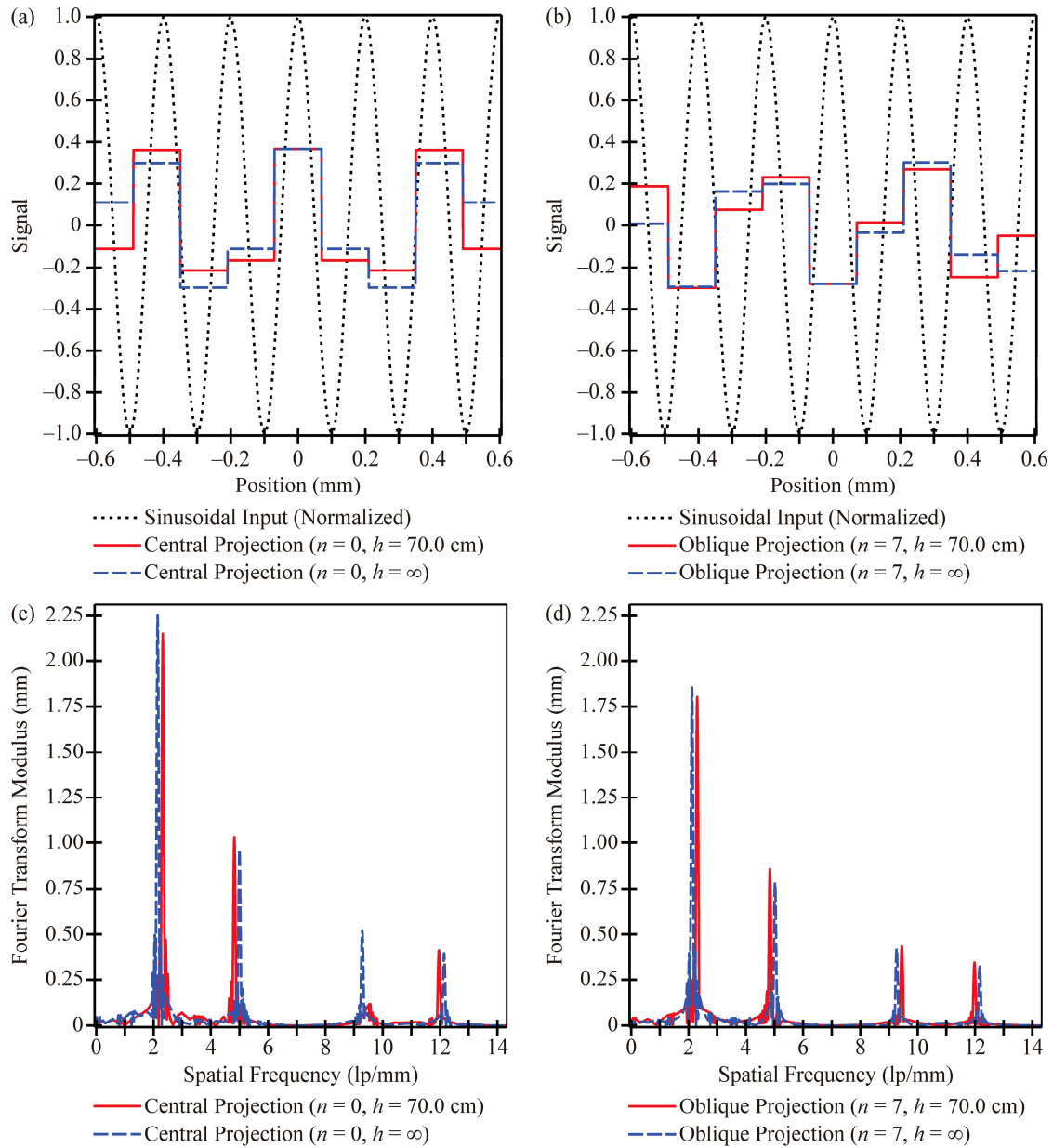
Figure 3. Assuming $N = 15$, $\Delta\psi = 1.07°$, $x_0 = 0$ mm, $z_0 = 25.0$ mm, $\varepsilon = 0.5$ mm, $a = 140$ μm, and $\nu_0 = 0.7a^{-1}$ (5.0 lp/mm), the output profiles of the central projection and the most oblique projection of a Selenia Dimensions DBT system are plotted versus position. In addition, continuous Fourier transforms are plotted versus spatial frequency.

its major peak at the input frequency. The major peak of the central projection, occurring at 2.32 lp/mm, is now highly suppressed in magnitude.

3.3 FBP Image Reconstruction

FBP reconstructions and their Fourier transforms are shown in Figure 4 at the height $z = z_0$, assuming that the filter truncation frequency ξ is 10 lp/mm. Although ξ is often specified to be the alias frequency $0.5a^{-1}$ (3.57 lp/mm), it is necessary to choose a higher value for the purpose of this work in order to achieve super-resolution.
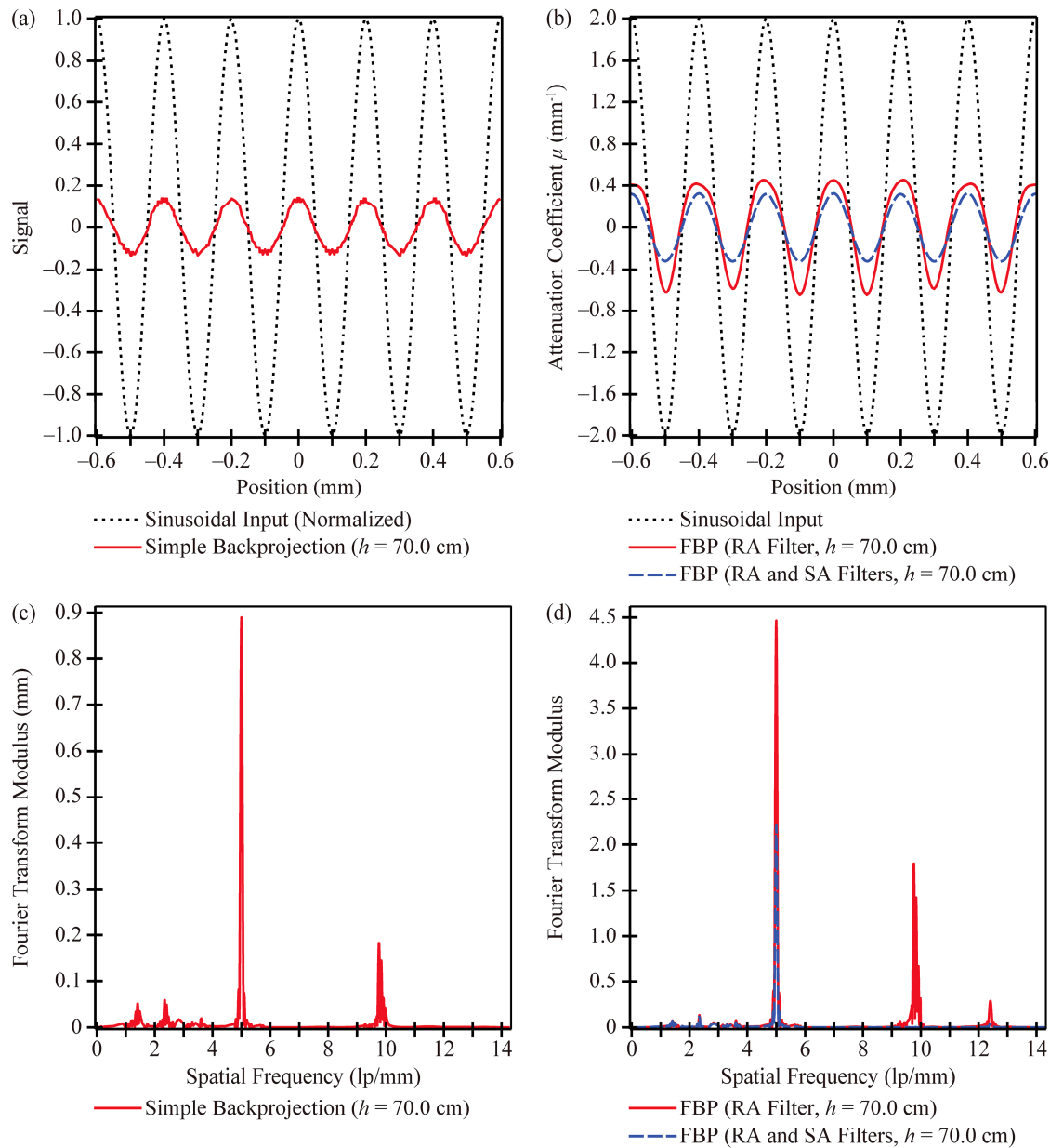
Figure 4. The SBP and FBP reconstructions are plotted in the spatial domain and the Fourier domain, assuming the same parameters as those used in Figure 3. Both the RA and the SA filters used in the FBP reconstruction are truncated at the frequency $\xi = 10$ lp/mm.

Figure 4 demonstrates that FBP reconstruction smoothens pixilation artifacts found in the SBP reconstruction, and further suppresses the magnitude of the alias peak at 2.32 lp/mm in the Fourier domain. In addition, Figure 4 indicates that reconstructing with the RA filter alone gives greater overall modulation than reconstructing with the RA and SA filters together. More specifically, the modulation for reconstruction with the RA filter alone is 28%, while the modulation for reconstruction with the RA and SA filters together is 17%. It is expected that the reconstruction with the RA filter alone has greater modulation, since the SA filter places more weight on low frequencies to reduce high frequency noise. Importantly, the modulation of either FBP reconstruction technique is well above the limit of resolution for typical imaging systems, which is often taken to be 5%. In addition, the modulation of either FBP reconstruction technique is greater than that of SBP reconstruction (14%).

Although reconstruction with the RA filter alone has the benefit of a higher modulation than reconstruction with the RA and SA filters together, the trade-off is greater spectral leakage at very high frequencies, such as those exceeding the input frequency 5.0 lp/mm. In fact, reconstruction with the RA filter alone has even more spectral leakage at very high frequencies than reconstruction with SBP. For example, the ratio of the amplitude of the alias peak at 9.75 lp/mm against that of the major peak at 5.0 lp/mm is 39.3% for FBP reconstruction with the RA filter alone and 22.1% for SBP. The reason for the increased high frequency spectral leakage is that the RA filter tends to amplify noise occurring at high frequencies. Recall that even with no shot noise or anatomical noise, a pixilated detector has an intrinsic white noise power spectrum (NPS) given by the product of the x-ray fluence with the square of the detector element length [11-13].

The high frequency spectral leakage that occurs in reconstructing with the RA filter alone generates flattening artifacts in the peaks of the reconstruction in the spatial domain (for example, see the peak at $r = \pm 0.40$ mm). The offset of the reconstructed waveform effectively appears downshifted from zero as a result. The reconstruction with both the RA and SA filters possesses less high frequency spectral leakage, and has fewer flattening artifacts in the spatial domain.

4. DISCUSSION AND CONCLUSION

In DBT, oblique x-ray incidence in the projections shifts the image of the object under study in sub-pixel increments along the detector. This work is novel in describing DBT's potential for super-resolution as a result of this property. Super-resolution has been shown to improve the visualization of line pairs in a bar pattern phantom. A theoretical framework for investigating super-resolution analytically has also been developed by calculating the reconstruction of a sinusoidal input. It is demonstrated that a reconstruction can resolve frequencies higher than the alias frequency of the detector, unlike a single projection which represents the information as a lower frequency.

In the analytical model, FBP reconstruction of the sinusoidal input was performed either with the RA filter alone or with both the RA and SA filters. Although reconstruction with the RA filter alone has the benefit of greater overall modulation in the spatial domain, it presents the drawback of increasing the presence of high frequency noise. As a result, the RA filter generates more high frequency spectral leakage in the Fourier domain, as well as more flattening artifacts in the spatial domain. High frequency spectral leakage is even more pronounced in reconstructing with the RA filter alone than in reconstructing with SBP. Reconstruction with both the RA and SA filters together has the greatest suppression of high frequency noise in the Fourier domain and the fewest flattening artifacts in the spatial domain.

Super-resolution is a particularly useful property because of the detector element binning that occurs in many clinical imaging systems that switch between DM mode and DBT mode. For example, in the Selenia Dimensions system, the DM detector element dimensions are 70 μm × 70 μm, while the DBT detector element dimensions are 140 μm × 140 μm. Binning has the effect of reducing the readout time for the DBT scan, which has multiple projections. The trade-off of binning is that the effective alias frequency of the detector is lowered. Although it would seem that detector element binning would make DBT less capable of resolving microcalcifications and other subtle signs of breast cancer, the existence of super-resolution in the reconstruction may counteract the drawback of a smaller alias frequency. For this reason, super-resolution has significant potential for many future applications in breast imaging.

Some of the limitations of this paper and directions for future modeling are now addressed. One limitation of this work is that MTF degradation with increasing angles of incidence θ_n relative to the normal has not been modeled [14-16]. Analytical models for the point spread function (PSF) and MTF of a-Se for non-normal x-ray incidence have been proposed by Que and Rowlands [5] and later verified with Monte Carlo simulations by Hajdok and Cunningham [17]. For more thorough modeling, the PSF of a-Se should be convolved with Eq. (9) to give signal intensity versus position r along the detector before detector element sampling is performed. As stated in the Methods sections, this rigorous modeling is not critical for measurements along the chest wall, since the angle of incidence does not deviate considerably from the normal and the MTF is no less than 96.6% for 20 keV x rays. However, at the corners of the detector opposite the chest wall, the angle of incidence deviates more considerably from the normal. For example, in the Selenia Dimensions detector (28.7 cm × 25.1 cm), the angle of incidence relative to the normal for many projections can be as high as 20°. For 200 μm thick a-Se and 20 keV x rays, one can show that the MTF for $\theta_n = 20°$ is 90.5% at 5.0 lp/mm and is 80.6% at 7.5 lp/mm. In imaging these frequencies at the corner of the detector, the MTF degradation should indeed be modeled.

The analytical models of this paper can furthermore be refined by using polynomial filters which have been shown to generate superior reconstructions to the conventional RA and SA filters [18, 19]. Also, shot noise and anatomical noise can be incorporated into the modeling [20, 21], and the orientation of the input sinusoidal waveform in 3D space can be made more general. In addition, the MTF degradation with increasing focal spot size and increasing focal spot motion during a continuous scan of the projections can be carefully considered [8, 22].

As a final extension of our current work, it would be useful to transition from simulating a pure sinusoidal input to simulating an array of microcalcification clusters in a breast-like background [23, 24]. One could then assess whether super-resolution allows model observers to distinguish finer morphological details than would otherwise be visible without super-resolution. Having greater insight into the fine structural details of the microcalcifications would yield useful diagnostic information about their pathology [25].

5. ACKNOWLEDGEMENT

6. REFERENCES

[1] Rafferty E. Tomosynthesis: New Weapon in Breast Cancer Fight. Imaging Economics. 2004;17(4).
[2] Park SC, Park MK, Kang MG. Super-resolution Image Reconstruction: A Technical Overview. IEEE Signal Processing Magazine. 2003;20(3):21-36.
[3] Albert M, Beideck DJ, Bakic PR, Maidment ADA. Aliasing effects in digital images of line-pair phantoms. Medical Physics. 2002;29(8):1716-8.
[4] Barrett HH, Myers KJ. Chapter 3: Fourier Analysis. In: Saleh BEA, editor. Foundations of Image Science. New York, NY: John Wiley & Sons; 2004. p. 95-174.
[5] Que W, Rowlands JA. X-ray imaging using amorphous selenium: Inherent spatial resolution. Medical Physics. 1995;22(4):365-74.
[6] Barrett HH, Myers KJ. Chapter 4: Series Expansions and Integral Transforms. In: Saleh BEA, editor. Foundations of Image Science. New York, NY: John Wiley & Sons; 2004. p. 175-214.
[7] Epstein CL. Introduction to the Mathematics of Medical Imaging. 2nd ed. Philadelphia: SIAM; 2008.
[8] Zhao B, Zhao W. Three-dimensional linear system analysis for breast tomosynthesis. Medical Physics. 2008;35(12):5219-32.
[9] Mertelmeier T, Orman J, Haerer W, Dudam MK. Optimizing filtered backprojection reconstruction for a breast tomosynthesis prototype device. In: Flynn MJ, Hsieh J, editors. Physics of Medical Imaging; 2006; San Diego: SPIE; 2006.
[10] Wolbarst AB. Chapter 30: Resolution and Magnification. Physics of Radiology. 2nd ed. Madison, WI: Medical Physics Publishing; 2005. p. 333-40.
[11] Albert M, Maidment ADA. Linear response theory for detectors consisting of discrete arrays. Medical Physics. 2000;27(10):2417-34.
[12] Acciavatti RJ, Maidment ADA. An Analytical Model of NPS and DQE Comparing Photon Counting and Energy Integrating Detectors. In: Samei E, Pelc NJ, editors. Physics of Medical Imaging; 2010; San Diego, CA: SPIE; 2010. p. 1-12.
[13] Acciavatti RJ, Maidment ADA. A Comparative Analysis of OTF, NPS, and DQE in Energy Integrating and Photon Counting Digital X-ray Detectors. Medical Physics. 2010;37(12):6480-95.

[14] Badano A, Kyprianou IS, Sempau J. Anisotropic imaging performance in indirect x-ray imaging detectors. Medical Physics. 2006;33(8):2698-713.

[15] Mainprize JG, Bloomquist AK, Kempston MP, Yaffe MJ. Resolution at oblique incidence angles of a flat panel imager for breast tomosynthesis. Medical Physics. 2006;33(9):3159-64.

[16] Acciavatti RJ, Maidment ADA. Calculation of OTF, NPS, and DQE for Oblique X-Ray Incidence on Turbid Granular Phosphors. In: Martí J, editor. IWDM 2010; 2010 16-18 June 2010; Girona, Spain: Springer-Verlag; 2010. p. 436-43.

[17] Hajdok G, Cunningham IA. Penalty on the detective quantum efficiency from off-axis incident x rays. In: Yaffe MJ, Flynn MJ, editors. Medical Imaging 2004: Physics of Medical Imaging; 2004; San Diego: SPIE; 2004. p. 109-18.

[18] Kunze H, Haerer W, Orman J, Mertelmeier T, Stierstorfer K. Filter determination for tomosynthesis aided by iterative reconstruction techniques. 9th International Meeting on Fully Three-Dimensional Image Reconstruction in Radiology and Nuclear Medicine; 2007 July 9-13; Lindau, Germany; 2007. p. 309-12.

[19] Lauritsch G, Harer WH. A theoretical framework for filtered backprojection in tomosynthesis. Imaging Processing; 1998; San Diego: SPIE; 1998. p. 1127-37.

[20] Barrett HH, Myers KJ. Chapter 12: Noise in Detectors. In: Saleh BEA, editor. Foundations of Image Science. New York, NY: John Wiley & Sons; 2004. p. 701-800.

[21] Hu Y-H, Masiar M, Zhao W. Breast Structural Noise in Digital Breast Tomosynthesis and Its Dependence on Reconstruction Methods. In: Martí J, editor. IWDM 2010; 2010 16-18 June 2010; Girona, Spain: Springer-Verlag; 2010. p. 598-605.

[22] Johns HE, Cunningham JR. Chapter 16: Diagnostic Radiology. The Physics of Radiology. 4th ed. Springfield, IL: Charles C Thomas; 1983. p. 557-669.

[23] Bakic PR, Albert M, Brzakovic D, Maidment ADA. Mammogram synthesis using a 3D simulation. I. Breast tissue model and image acquisition simulation. Medical Physics. 2002;29(9):2131-9.

[24] Zhang C, Bakic P, Maidment ADA. Development of an anthropomorphic breast software phantom based on region growing algorithm. In: Miga MI, Cleary KR, editors. Medical Imaging 2008; 2008; San Diego: SPIE; 2008. p. 1-10.

[25] Lanyi M. Chapter 7: Differential Diagnosis of Microcalcifications. Diagnosis and Differential Diagnosis of Breast Calcifications. Berlin: Springer-Verlag; 1988. p. 193-231.